Journal of Molecular Graphics and Modelling 27 (2008) 356–363

Contents lists available at ScienceDirect

Journal of Molecular Graphics and Modelling

journal homepage: www.elsevier.com/locate/JMGM

Atomistic modelling of crack propagation in a randomly rough nano-scale metallic surface

Sh. Behzadi [a], H. Rafii-Tabar [a,b,c,*]

[a] Computational Physical Sciences Research Laboratory, Department of Nano-Science, Institute for Research in Fundamental Sciences (IPM), P.O. Box 19395-5531, Tehran, Iran
[b] Department of Medical Physics and Biomedical Engineering, Shahid Beheshti University of Medical Sciences, Evin, Tehran, Iran
[c] Research Centre for Nano-Technology and Tissue Engineering, Shahid Beheshti University of Medical Sciences, Evin, Tehran, Iran

ARTICLE INFO

Article history:
Received 20 February 2008
Received in revised form 10 June 2008
Accepted 13 June 2008
Available online 24 June 2008

Keywords:
Rough surface
Crack propagation
Fractional Brownian motion
Sutton–Chen potential

ABSTRACT

Molecular dynamics simulations, based on many-body interatomic potentials, are performed to investigate the propagation of a Mode-I (edge) crack in a roughened two-dimensional (2D) (1 1 1) plane of a generic lattice for which we adopt the potential parameters pertinent to the elemental Ag. The randomly rough surface is generated with the help of a fractal-based technique referred to as fractional Brownian motion method. We show that fluctuations in the crack velocity, which lead to the phenomenon of crack branching, are also present for crack propagation in rough surfaces. However, as the roughness increases, this phenomenon becomes less pronounced, and another type of velocity fluctuation associated with the roughness of the surface emerges. Furthermore, it is found that as the roughness of the surface increases, the critical stress for the initiation of crack propagation is increased, and the fluctuations in the crack velocity make their appearance sooner.

1. Introduction

A material surface forms an interface between two, often very different, condensed phases, and has a far more complex structure than that represented by a simple geometric boundary. Close examination of solid surfaces by instruments such as the scanning tunnelling microscope (STM) reveals that material surfaces are quite *rough* on atomic and molecular scales, and they are decorated with all types of irregular structures located along all directions. The roughness is generated by *random*, short wave-length, fluctuations in the atomic architecture of the surface, and is characterised by the presence of nano- and meso-scale hills and valleys of various sizes, shapes, contact angles and densities. These hills are called surface *asperities*, and form localised stochastic structures composed of several hundred to several million atoms or molecules. They can appear on the surfaces of metals, polymers, ceramics and carbon-based materials [1], and their spatial distribution can be either directional or homogeneous in all directions. From a nanoscopic, or mesoscopic, perspective, therefore, an apparently smooth material surface can have a very complex texture consisting of a multitude of asperities of various sizes and shapes. The physical properties of such rough surfaces are, therefore, far more complex than those corresponding to a simple continuum-based *mirror-like* topography.

When two rough surfaces come into close proximity, they form a solid-state *junction* under an applied load, and the actual contact between them takes place over the tips of their respective asperities. Therefore, their *apparent* area of contact is considerably different from their *real* area of contact. The asperities on the contacting rough surfaces experience highly localised stresses in the ultra-small volume of material located at the tips, and the size of the initial regions of contact is, therefore, determined by the stress–strain properties of these asperities during contact.

On the surface, and even sub-surface, areas of the asperities on a material surface subject to an applied load, plastic flow can lead to nucleation of a considerable number of dislocations, and these dislocations multiply and grow in concentration with an increase in the load. The dislocations generated on the surface and near-surface regions can penetrate into the bulk, locally coalescing, producing weak zones within the material where cracks and voids can nucleate and multiply. These cracks can propagate from the sub-surface to the surface region, producing *wear particles* from the asperities.

We can, therefore, state that the response characteristics of rough surfaces control, in a very fundamental way, the tribological, adhesion, fracture, and wear properties of materials on macroscopic scales.

* Corresponding author at: Computational Physical Sciences Research Laboratory, Department of Nano-Science, Institute for Research in Fundamental Sciences (IPM), P.O. Box 19395-5531, Tehran, Iran. Tel.: +98 2122835061; fax: +98 2122835058.
E-mail address: rafii-tabar@nano.ipm.ac.ir (H. Rafii-Tabar).

1093-3263/$ – see front matter © 2008 Elsevier Inc. All rights reserved.
doi:10.1016/j.jmgm.2008.06.005

One research area of interest is, therefore, the study of crack propagation in randomly rough nano-scale surfaces subject to an externally applied stress. Crack propagation in *smooth* nano-scale surfaces has been investigated in a large number of modelling and experimental studies, reviewed in Refs. [2,3]. Several nanoscopic modelling studies have shown that although the continuum-based theories of elasticity can provide valuable insights into the dynamics of fracture processes, they cannot account for many of the crack characteristics observed experimentally. For example, these theories predict that the topography of the crack surfaces is smooth and mirror-like, and that the limiting crack speed is equal to the Rayleigh surface wave velocity V_R of the material. Experimental evidence, however, suggests that crack surfaces that are initially mirror-like undergo a very clear *mirror-to-mist-to-hackle* roughening transition, and that the maximum crack velocity is 0.6 V_R. The experimental results also show that a *dynamic* instability emerges in the crack velocity when it exceeds 0.36 V_R. The manifestation of this instability is that the crack dynamics change dramatically, and the crack mean acceleration drops, leading to strong oscillations in crack velocity and *bifurcation* of crack trajectory (crack branching), and the appearance of rough crack surfaces. This instability has also been predicted in a modelling study [4] in which the surface contains various forms of impurities. These highly exotic phenomena are unexplained by continuum-based theories, but have been successfully accounted for in atomistic-based modelling studies [2,3].

In this paper, we have investigated, for the first time, Mode-I crack propagation in a rough (1 1 1) plane. The 2D plane is generic, and in the actual computation with this plane, we have assumed the potential parameters for the elemental Ag. This lattice could be viewed as representing a model system for a brittle crystal. We have employed molecular dynamics (MD) simulation method using an accurate many-body interatomic potential. The organisation of this paper is as follows. In Section 2, the computational method employed for generating a randomly rough surface at the nano-scale is described. In Section 3, the details of the MD simulation, including a brief description of the interatomic potential, and the derivation of the atomic-scale stress tensor are given. This is followed by a description and discussion of the results in Section 4. We will see that the basic laws underlying crack propagation in smooth surfaces generally also hold for crack propagation in rough surfaces.

2. Generation of a randomly rough surface via fractional Brownian motion method

There are basically three models available for generating a randomly rough surface. The first model is the random process model (RPM), originally proposed by Rice [5], and based on the analysis of a random noise signal. This model was further generalised [6] by including the evaluation of the actual distribution of heights of the profile peaks and summits and their corresponding curvatures, leading to a better understanding of the behaviour of the surface profile wherein the model is described in terms of three parameters, namely, height, slope and the curvature of either a peak or a summit. The second model is the curve-fitting model (CFM) [7] in which there is a set of n points with coordinates (x_i, h_i), $i = 1, \ldots, n$, where h_i are the heights at positions x_i. From these points, a function $f(x)$ is determined so that $f(x_i) \approx h_i$. The type of $f(x)$ used depends on the problem under study. Two of the most important types of $f(x)$ used are a polynomial of a certain degree and a Fourier series. The details of these functions can be found in Ref. [7]. The third model is the fractal model. In general, fractal geometry was motivated by such objects whose topography could not be characterised by Euclidean geometry, and required fractional dimensions. Furthermore, a fractal is based on the concept of self-similarity wherein each segment of the structure is similar to the whole of the structure. One such object is a rough material surface, since if such a surface is continuously magnified, the details of its roughness re-occur and the surface profile is never smooth [8].

We employ a version of the surface fractal model, generated via the method that is referred to as the fractional Brownian motion (FBM). We use the fractal model of a rough surface since it is more appropriate for generating a rough surface at nano-scales, whereas the RPM is better at generating rough surfaces with micron-sized asperities, and the CFM is more suitable for modelling rough surfaces that are in contact since, as a result of wear and plastic deformation during contact, the topographies of these surfaces transform into structures that are better described by a curve.

It has been proposed [9] that Brownian dynamics can be used to generate a fractal structure from a set of samples. The FBM method is based on the use of Brownian dynamics to generate an irregular, self-similar, fractal-type rough surface with a known fractional dimension. The FBM is described by the mean-square displacement between two heights

$$\langle |\mathbf{h}_i - \mathbf{h}_j|^2 \rangle \approx \mathbf{d}_{ij}^{2H}, \tag{1}$$

where $\mathbf{h}_i$, $\mathbf{h}_j$ and $\mathbf{d}_{ij}$ are respectively the height vectors at positions (x_i, y_i) and (x_j, y_j) on the two-dimensional surface, and the spatial distance between these two points, H is the Hurst exponent that describes the type of correlation [10]. When $H > (1/2)$, the correlation in the successive steps of the FBM is positive, whereas when $H < (1/2)$, this correlation is negative. For $H = (1/2)$, the successive steps in the trajectory of the FBM are uncorrelated, implying that for this value of H, one obtains the standard Brownian motion.

Eq. (1) is the power-law representation of long-range correlations [11]. The Hurst exponent is related to the fractal dimension D via [9]

$$D = 3 - H. \tag{2}$$

It is evident from Eq. (2) that the smaller the parameter H, the larger is D, and hence the more irregular (or more rough) the surface becomes.

One practical way to generate long-range correlations, such as that represented by (1), is by employing their spectral density $S(\mathbf{q})$ which is the Fourier transform of their covariance. If the dimension of the FBM is η, then this density is given by [10]

$$S(\mathbf{q}) = \frac{a(\eta)}{\left(\sum_{i=1}^{\eta} q_i^2\right)^{H+(\eta/2)}}, \tag{3}$$

where $\mathbf{q} = (q_1, \ldots, q_\eta)$ is the wave vector, and $a(\eta)$ is an η-dependent constant. By employing the fast Fourier transform technique, Eq. (3) can be used to generate an FBM array consisting of correlated numbers satisfying Eq. (1) via the following steps [10]:

1. Random numbers are generated uniformly with an RMS = 0.5. These numbers are then assigned to the sites on a d-dimensional lattice representing the material structure, such as the surface
2. The random numbers generated in step (1) form an η-dimensional array whose Fourier transform is then calculated numerically. The results obtained are then multiplied by $\sqrt{S(\mathbf{q})}$
3. An inverse Fourier transform is applied to the results from step (2). This leads to an array of numbers that are correlated and

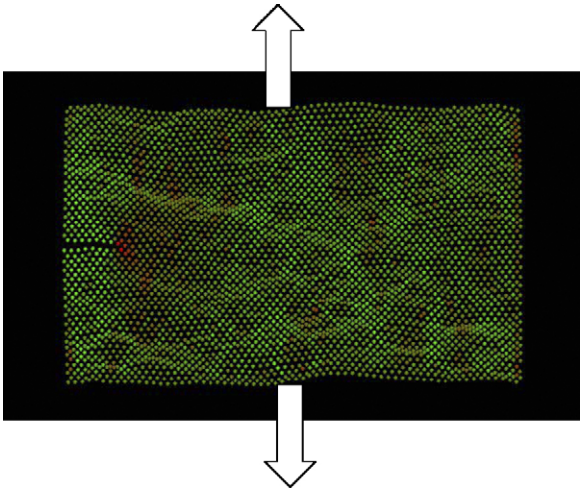

Fig. 1. The roughened (1 1 1) plane of an fcc lattice with $H = 0.7$, showing the initial inserted Mode-I crack, and the loading condition. The red colour refers to the atoms that are more stressed.

satisfy Eq. (1), and they act as the heights of the asperities in our model of the rough surface.

Since the use of the Fourier transform can impose a periodicity on the array, which is problematical, in order to avoid this, we should generate an array of a much larger size than the array that is actually to be employed in the simulation of the physical system under consideration. This procedure, however, reduces the accuracy of the fast Fourier transform, and hence one can handle only small systems with this method. In our case, we deal with a nano-scale surface, and hence this method of generating a rough surface is suitable. Fig. 1 shows a (1 1 1) plane of a generic lattice that has been transformed into a rough surface with the use of the FBM method. We have investigated the propagation of an inserted crack in this plane.

3. Details of the MD simulation

3.1. Interatomic potential

The MD simulations performed in this paper were based on the many-body Sutton and Chen (SC) interatomic potentials [12]. These potentials were constructed for the description of the energetics and dynamics of the ten fcc elemental metals. They were specifically designed for use in computer-based simulations relating to the mechanical properties of materials. In these potentials, the total energy is written as

$$H_I^{\mathrm{SC}} = \epsilon \left[\frac{1}{2} \sum_i \sum_{j \neq i} V(r_{ij}) - c \sum_i \sqrt{\rho_i} \right], \tag{4}$$

and

$$V(r_{ij}) = \left(\frac{a}{r_{ij}} \right)^n, \qquad \rho_i = \sum_{j \neq i} \left(\frac{a}{r_{ij}} \right)^m, \tag{5}$$

where ϵ is a parameter with dimensions of energy, a is a parameter with dimensions of length and is normally taken to be the equilibrium lattice constant, m and n are positive integers with $n > m$. The SC potentials are of the Finnis and Sinclair [13] many-body interatomic potential type, and are, therefore, similar in *form* to the embedded atom potential (EAM) [14].

The *power-law* form of the potential terms was adopted in order to construct a unified potential that combines the short-range interactions, represented by the many-body second term in Eq. (4), with a van der Waals tail that gives a better description of the interactions at the long range. For a particular fcc metal, the potential in Eq. (4) is completely specified by the values of m and n, since the equilibrium lattice condition fixes the value of c. The values of the potential parameters, computed for a cut-off radius of 10 lattice constants, are given in Ref. [12]. This potential, and its generalisation for the description of fcc metallic alloys [15], have been extensively applied in modelling a range of material properties at nano-scales, and the results have shown reasonable agreement with the experimental data.

3.2. Atomic-site stress field

In the simulation of crack propagation in an atomic lattice, the determination of the location and velocity of the *crack tip* is essential. These two variables can be computed once the atom representing the crack tip is identified. *The crack tip at each simulation time-step corresponds to the atom that experiences the highest local stress*. It is, therefore, necessary to obtain a map of the stress distribution at *each atomic site* in a lattice composed of N atoms, at each simulation time-step.

The concept of an atomic-level stress field computed over atomic sites is described by a rank-two tensor $\sigma_{\alpha\beta}(i)$, where i refers to a particular atom in the N-body lattice, and $\alpha = 1, 2, 3$ and $\beta = 1, 2, 3$ refer to the Cartesian coordinates. This tensor was originally developed by Born and Huang [16], using the technique of small homogeneous deformations. By applying small displacements to a pair of atoms i and j, with an initial separation of r_{ij}, it has been shown [16] that the Cartesian components of this stress tensor at atomic sites are given by

$$\sigma_{\alpha\beta}(i) = \frac{1}{2\Omega_i} \sum_{j>i} \frac{\partial \Phi(r_{ij})}{\partial r_{ij}} \frac{(r_{ij})_\alpha (r_{ij})_\beta}{r_{ij}}, \tag{6}$$

where $\Phi(r_{ij})$ are the pair-wise interatomic potentials describing the interactions in the N-body system, and Ω_i is the local atomic volume which can be identified with the volume of the Voronoi polyhedron associated with the atom i [17]. This expression has also been explicitly derived [18] and has been used in a series of papers [19,20] dealing with the local structural fluctuations in amorphous and liquid metals.

Eq. (6) provides the usual way of computing the stress field over each atomic site in MD simulations. Stress calculation in atomistic simulations can also be performed by computing the negative of the pressure tensor $P_{\alpha\beta}$, given [21] by

$$P_{\alpha\beta} = \frac{1}{V} \left(\sum_i^N \frac{p_{i\alpha}\, p_{i\beta}}{m_i} + \sum_{i=1}^N \sum_{j>i}^N (r_{ij})_\alpha (F_{ij})_\beta \right), \tag{7}$$

where p_i is the momentum of particle i, F_{ij} the force experienced by atom i due to atom j, and V is the volume of the many-body system. In Eq. (7), the first term normally refers to the contribution of the ideal gas [22], or the kinetic energy, part, and the second term refers to the contribution of the virial part. This pressure tensor is a multi-particle property and is, therefore, a property of the system as a whole, and so no additional averaging over the N particles is possible [21]. If this tensor were to be used to compute the stress field at each atomic site, then V should be replaced with Ω_i, as in Eq. (6), and the kinetic energy part, and the virial part, must also be computed for each individual atom i, i.e. the summations must only be taken over the atom j.

Comparison of the stress tensor calculation using Eqs. (6) and (7) shows that in the former case the contribution of the ideal gas part is not included in the computation of the atomic-site stress field in crystalline materials. As will be shown later, the computed contribution of the ideal gas part is negligible in the propagation of the cracks in a crystalline material.

Furthermore, a prescription for computing the stress field at a *point* in a crystal, and not at an atomic site, has also been given [23]. The previously stated pressure tensor technique, i.e. Eq. (7), and this latter technique of computing the stress field at a point, both contain the contribution of the kinetic energy part.

For the Sutton and Chen many-body potential, given in Eq. (4), the expression for atomic-site stress tensor Eq. (6) takes on the form (see also [24])

$$\sigma^{\mathrm{SC}}_{\alpha\beta}(i) = \frac{\epsilon}{2a^2\Omega_i}\sum_{j\neq i}\left[-n\left(\frac{a}{r_{ij}}\right)^{n+2} + cm\left(\frac{1}{\sqrt{\rho_i}}+\frac{1}{\sqrt{\rho_j}}\right)\left(\frac{a}{r_{ij}}\right)^{m+2}\right] r^{\alpha}_{ij} r^{\beta}_{ij}. \tag{8}$$

We will see later on that in our simulation of the crack propagation, as the attendant temperatures are quite low, Eq. (8), wherein the contribution of the kinetic energy part is not included, is adequate for computing the stress field at each atomic site, for locating the atom corresponding to the crack tip.

The volumes Ω_i of individual atoms can be obtained by computing numerically their corresponding Voronoi polyhedra according to the prescription given in Ref. [21].

4. Results

4.1. Insertion of the initial Mode-I crack in the rough 2D lattice

We employed a 2D lattice, for computational convenience, allowed, however, to deform into the third dimension *z*. The lattice considered was triangular and *flat*, similar to the (1 1 1) plane of an fcc crystal. It was composed of 64 rows of atoms with 64 atoms per row. The flat lattice was equilibrated at a constant temperature of 0.01 K for 50,000 time steps dt, with dt = 5 fs, to obtain its minimum-energy configuration.

Following its equilibration, the lattice was *roughened* via the FBM method, described in Section 2. The roughened lattice was re-equilibrated for a further 50,000 dt for three cases, $H = 0.9, 0.8$, and 0.7. In the absence of an imposed constraint, the re-equilibration of the roughened surface would have restored the lattice to its original flat geometry. In order to preserve the rough geometry of the lattice during both the equilibration phase, and also during the actual simulation phase, a constraint in the *z*-direction was applied, i.e. the height functions h appearing in Eq. (1) were not allowed to change after their initial setting. This was achieved by switching off the interatomic interactions in the roughened lattice in the *z*-direction. This procedure implies that we obtain the minimum-energy state, i.e. the equilibrium state, for a rough lattice under a *specific* imposed constraint. Within the MD approach it is possible to obtain an equilibrium state under various boundary, or imposed, conditions. For example, in many MD-based simulations of such phenomena as nano-indentation, wherein a sharp tip approaches a flat substrate and either penetrates it or scan the surface while in contact, like the structure in an atomic force microscope (AFM), several layers of atoms of the substrate, and the tip, are usually modelled as static atoms, while other layers are treated as dynamic [2,3]. So, in many MD simulations a constraint can be applied to a part of the simulated system while the same constraint is not applied to other parts, and the system is brought into equilibrium under these specific conditions. It is within this approximate approach that we have considered the crack propagation in the roughened surface.

Furthermore, the procedure implies that the roughness of the lattice in our simulation was of a *static* type, which is an approximation to the true behaviour of an actual rough surface, wherein the roughness is dynamic and can fluctuate in the course of time even at room temperature. A dynamic roughness can also be implemented in an MD simulation by imposing such constraints as harmonic springs between atoms in the *z*-direction. We were motivated to adopt this static model of a rough surface, since our main concern was to examine the effect of the roughness in *general* on the propagation of a crack. It should be remarked that when we created a statically rough surface, we ensured that the atoms were still bonded together within the range of the lattice parameter, i.e. the protruding atoms were not suspended in the vacuum. The above constraint during equilibration was adopted throughout the course of simulation whenever it was necessary to equilibrate the system. Fig. 1 shows an example of the rough 2D surface generated for $H = 0.7$.

An initial edge crack of length 7d, where d is the triangular lattice constant (d = 2.89 Å), was then inserted into the roughened surface, as shown in Fig. 1, for the case $H = 0.7$. The insertion was performed in such a way so that the atoms on the two opposite edges of the crack planes did not interact with each other. The roughened surface containing the edge crack was then equilibrated for 50,000 dt.

4.2. Computation of the critical stress

In order to determine the critical stress σ_c for crack propagation, i.e. the equivalent of Griffith's load, the following procedure was adopted. The stress was expressed in *force per atom*, and the unit adopted was picoNewton/atom (pN/atom). This choice is due to the fact that the volume term Ω_i in Eq. (8), or V in Eq. (7) when it refers to a single atom, pertains to the *volume* of the atom. Therefore, the stress becomes force per area, so that the unit pN/atom refers to force per area which is the standard definition of the stress.

Initially, a constant stress of 10 pN/atom, i.e. a stress rate of 0.005 pN/(atom dt), was applied to the arrays of atoms on the upper and lower edges of the roughened plane in Mode-I loading, as shown in Fig. 1. This stress was applied while the system was being equilibrated. It was observed that the application of this rate of stress did not result in the further movement of the crack tip, but led to the further opening of the crack front, i.e. the crack opening displacement (COD) was increased. In the next step, the stress rate was increased to 0.01 pN/(atom dt), i.e. a further stress of 10 pN/atom was added to the previous applied stress, while the system was being equilibrated again. Since it was observed that the crack tip did not move forward, the procedure was repeated until it was observed that the crack tip moved forward. In order to fine-tune the critical stress value, the last added stress was reduced and then gradually increased by smaller steps than 10 pN/atom, until the exact value of the σ_c was obtained. The critical stress for various surface roughness index H is listed in Table 1.

In order to examine the effect of changing the applied stress rate on the value of σ_c, we also computed σ_c when the initial applied stress rate was set at 0.01 pN/(atom dt), i.e. a constant stress value of 20 pN/atom. The rate was then increased to 0.02 pN/(atom dt), by adding of a stress of 20 pN/atom, rather than 10 pN/atom, in the subsequent steps. A similar procedure to the above was followed to obtain the value of σ_c. These results are also listed in Table 1, and it can be seen that the critical stress value is slightly smaller for the higher stress rate.

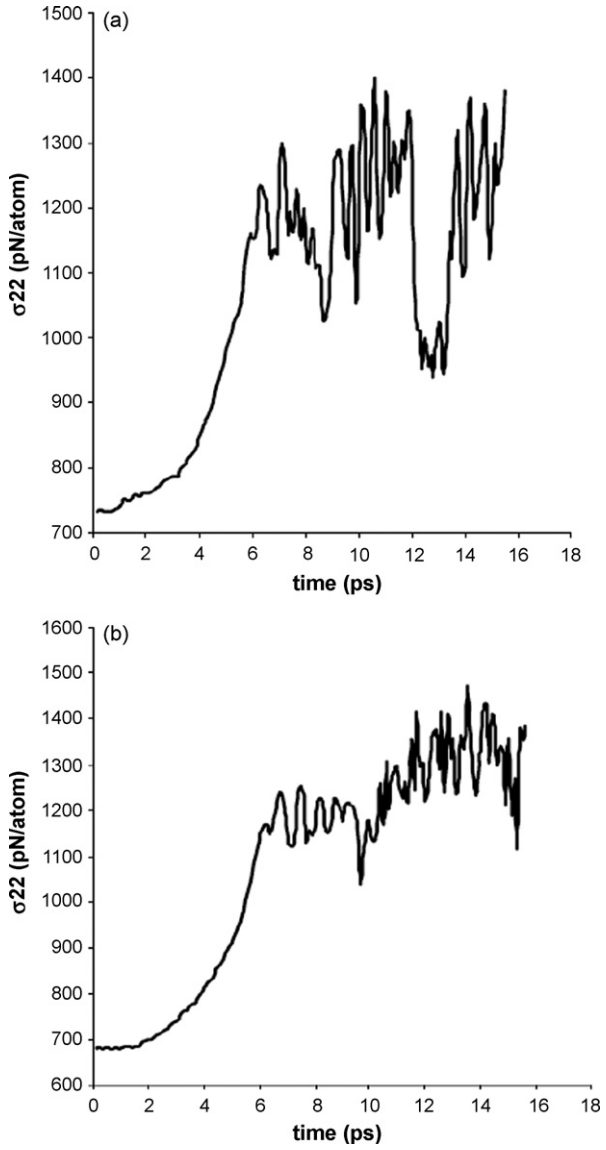

Fig. 2. The time evolution of the stress field at the crack-tip atom at stress rate of 1: (a) $H = 0.7$; (b) $H = 0.9$. It can be observed that as the roughness of the surface increases, the fluctuations in the stress become more pronounced.

These data should be compared with the critical stress for the propagation of crack in a smooth surface, which has been computed [2] for a (1 1 1) flat plane to be $\sigma_c = 136.8$ pN/atom, which is close to the σ_c for the least rough surface, i.e. when $H = 0.9$. From the values of σ_c listed in Table 1, it is seen that the rougher the surface becomes, the greater is the value of the critical stress necessary to propagate the crack. It can be surmised that this phenomenon arises as a result of the extra potential barrier that an advancing crack must overcome when moving in a roughened surface.

Table 1
Variation of critical stress with the roughness index

H	σ_c (pN/atom)	σ_c (pN/atom)
0.9	137.5	137.3
0.8	139.3	139.0
0.7	141.1	140.9

The second and third columns refer respectively to the initial stress rates of 0.005 and 0.01 pN/atom.

4.3. Identification of the crack tip

As was stated above, the crack tip is identified with the atom experiencing the highest stress, since concentration of the stress at a crack tip is maximum [25]. Eq. (8) was used to provide the stress map at each atomic site during the crack propagation, and the atom with the highest value of stress was selected to represent the crack tip at each simulation time-step. The variations of the stress in the vicinity of the crack tip are shown in Fig. 2 for two different values of the surface roughness. We observe that, after a smooth rise in value, the stress underwent repetitive rises and falls to maximum and minimum values, and when crack branching, to be explained later, was taking place, these rises and falls were much more pronounced.

It is evident that in using Eq. (8) to compute the atomic-site stress field, we have neglected the contribution of the kinetic energy part, as given in Eq. (7). In order to justify the exclusion of this term, we performed a computation of the atomic-site stress field in the presence of this term. It was found that when the temperature of the system was allowed to evolve during the propagation of the crack, the contribution of this term was only 1% of the contribution of the virial term, i.e. the term in Eq. (8), even at the lowest value of the virial component, and at the highest value of the crack velocity.

4.4. Propagation and branching of the original crack

The crack was propagated by applying a stress rate, beyond the computed critical stress, for each value of H. This rate ranged from 0.025 to 1 pN/(atom ps). Beyond the critical stress, when the crack was advancing, the temperature of the system was no longer kept at a constant value, and was allowed to evolve so that *fluctuations* in the crack velocity, responsible for the appearance of crack branching [2,26,27], could manifest themselves. It has been shown that these fluctuations appear at a well-defined critical velocity which is independent of the sample geometry, sample thickness, the applied stress, and the acceleration rates of the crack tip. They arise because the mean acceleration of the crack drops sharply, leading to the oscillations in the velocity. The appearance of these oscillations coincides with the appearance of the jagged topologies on the fracture surfaces.

Figs. 3–5 show the variations of the crack velocity for three different values of H and for stress rates of 0.025, 0.1, and 1 pN/(atom ps). From these figures we can see that, just as in the case of crack propagation in a smooth surface [2], fluctuations also make their appearance here. However, in this case, we observe a larger

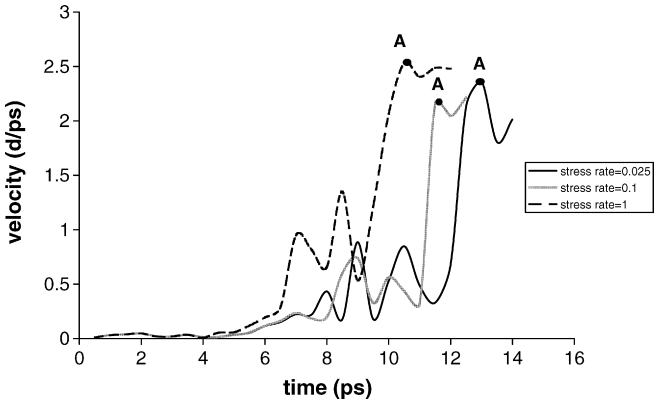

Fig. 3. The variations of the crack velocity for three different values of stress rates, 0.025, 0.1, and 1, with $H = 0.9$. We can observe that as the stress rate increases, the crack branching takes place sooner.

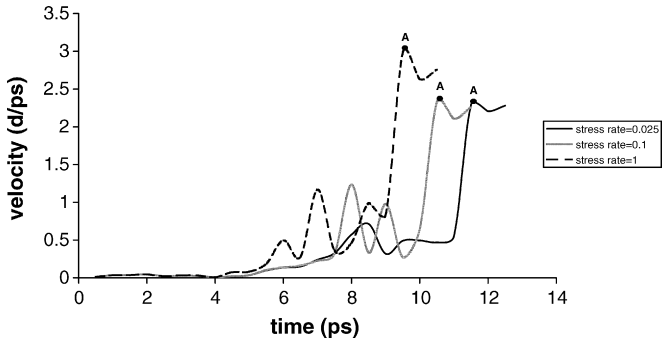

Fig. 4. The variations of the crack velocity for three different values of stress rates, 0.025, 0.1, and 1, with $H = 0.8$. We can observe that as the stress rate increases, the crack branching takes place sooner.

number of fluctuations in the velocity profiles. We refer to the fluctuations appearing before points A on all these profiles as the *early* fluctuations, and these arise as a result of the *roughness* of the surface, as they were not observed in the case of crack propagation in a smooth surface. While these early fluctuations do not lead to crack branching, those fluctuations beyond points A are associated with the onset of branching of the original crack. The crack branching was observed at velocities in the range of 2–3 *d* / ps. This range is about 30.5% of the shear-wave speed V_S, or about 32% of the Rayleigh surface wave speed V_R, where these are given by [28]

$$V_S = \sqrt{\frac{E}{2\rho(1+\nu)}}, \qquad V_R = V_S \frac{0.862 + 1.14\nu}{1+\nu}, \tag{9}$$

where ρ is the mass density, ν is Poisson's ratio, and E is Young's modulus. Consequently, from Figs. 3–5, we see that following the early fluctuations, the crack accelerates smoothly, but when the velocity reaches about one-third of V_R, it undergoes erratic oscillations with an amplitude of about 10% of the highest crack velocity, resulting in the appearance of crack branching and the roughening transition of the crack surfaces. A similar result was also obtained for the crack propagation in a smooth surface [2]. Our results, together with those obtained for crack propagation in a smooth surface, indicate that we can attribute the bifurcation in the crack dynamics to the behaviour of the crack velocity, rather than to the quasi-stress intensity factor of the propagating crack.

Another conclusion that can be drawn from an examination of Figs. 3–5 is that for any stress rate, for example 0.025 pN/(atom ps), the more the roughness of the surface increases, the less time it takes for the velocity fluctuations, both the early and those associated with

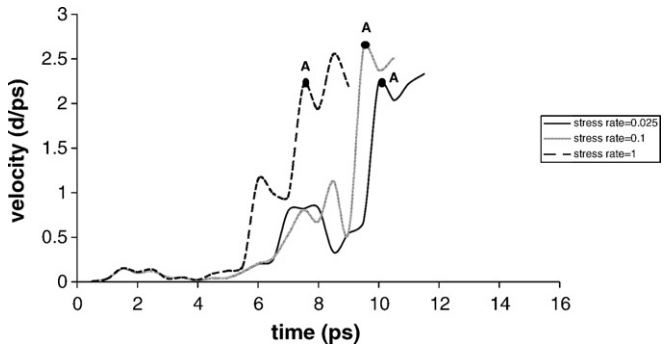

Fig. 5. The variations of the crack velocity for three different values of stress rates, 0.025, 0.1, and 1, with $H = 0.7$. We can observe that as the stress rate increases, the crack branching takes place sooner.

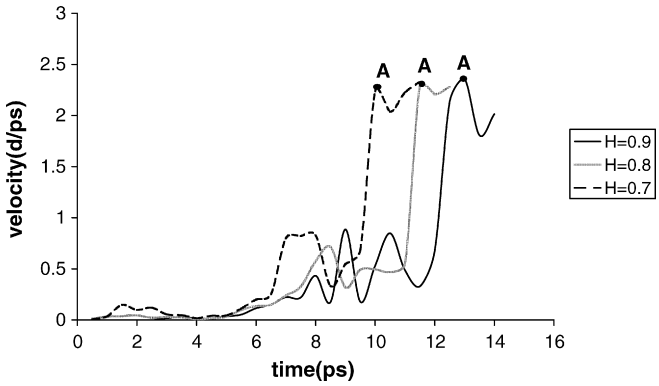

Fig. 6. Comparison of variations of crack velocities for three different surface roughness, $H = 0.7$, 0.8, and 0.9 at the same stress rate 0.025. It is evident that the rougher the surface, the less time it takes for velocity fluctuations to appear and, hence, the less time it takes for crack branching to make its appearance.

branching, to make their appearance, and hence the quicker crack branching takes place. Fig. 6 compares the fluctuations for different surface roughness, but at the same stress rate.

Figs. 7–9 show the simulation snapshots of the crack propagation at three different time steps, i.e. after 12, 19, and 25.5 ps, and for three different values of *H*. As can be seen from these figures, and comparing like figures, we see that the topography of the crack surfaces is different for different values of the roughness. This is particularly true when the crack has propagated for some time, e.g. as in Figs. 7c, 8c, and 9c.

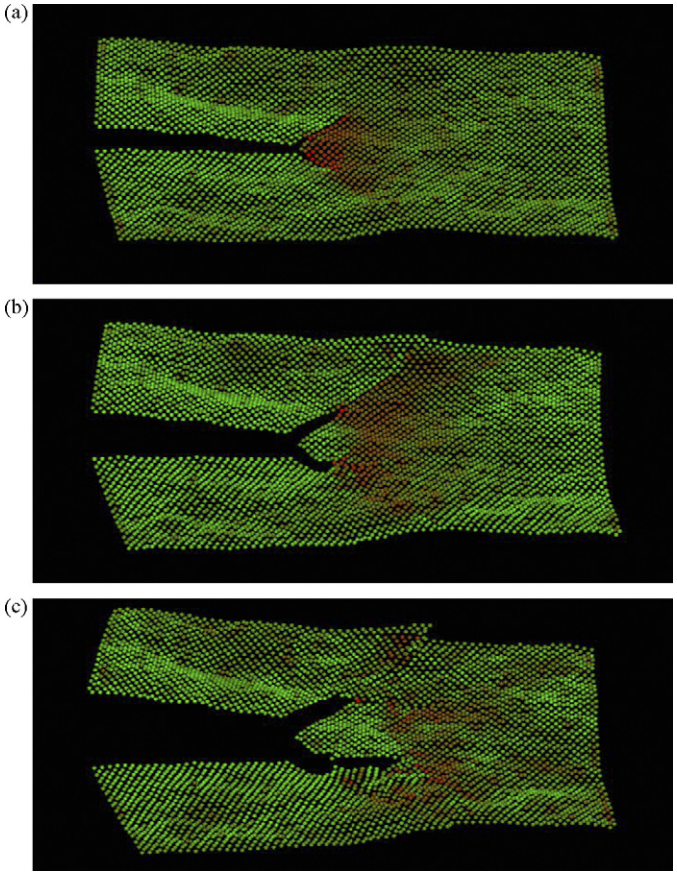

Fig. 7. Simulation snapshot of the crack propagation at three different time steps: (a) after 12 ps; (b) 19 ps; (c) 25.5 ps, with $H = 0.9$. This figure corresponds to Fig. 3 for stress rate equals to 1. The colour code is the same as Fig. 1.

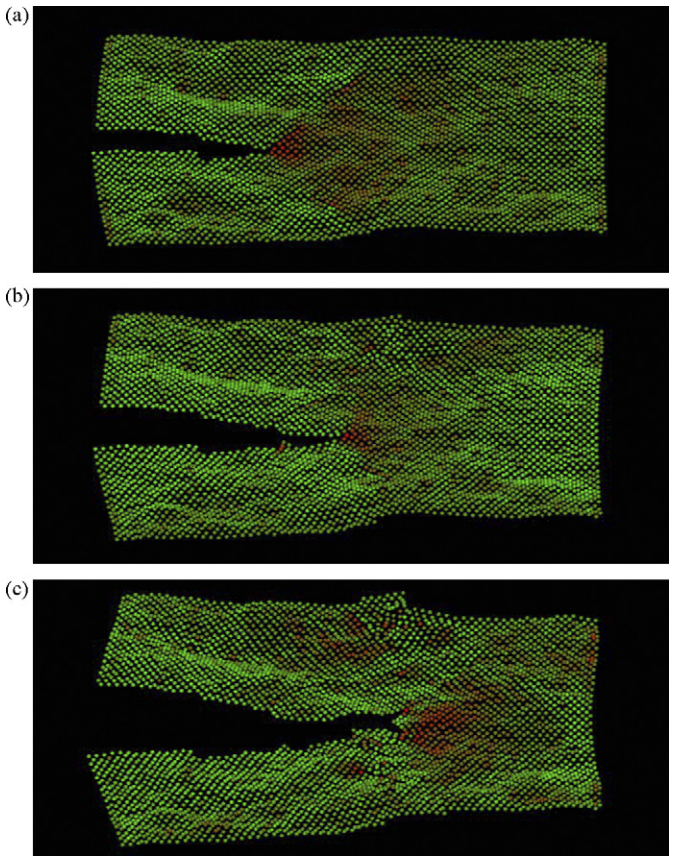

Fig. 8. Simulation snapshot of the crack propagation at three different time steps: (a) after 12 ps; (b) 19 ps; (c) 25.5 ps, with $H = 0.8$. This figure corresponds to Fig. 4 for stress rate equals to 1. The colour code is the same as Fig. 1.

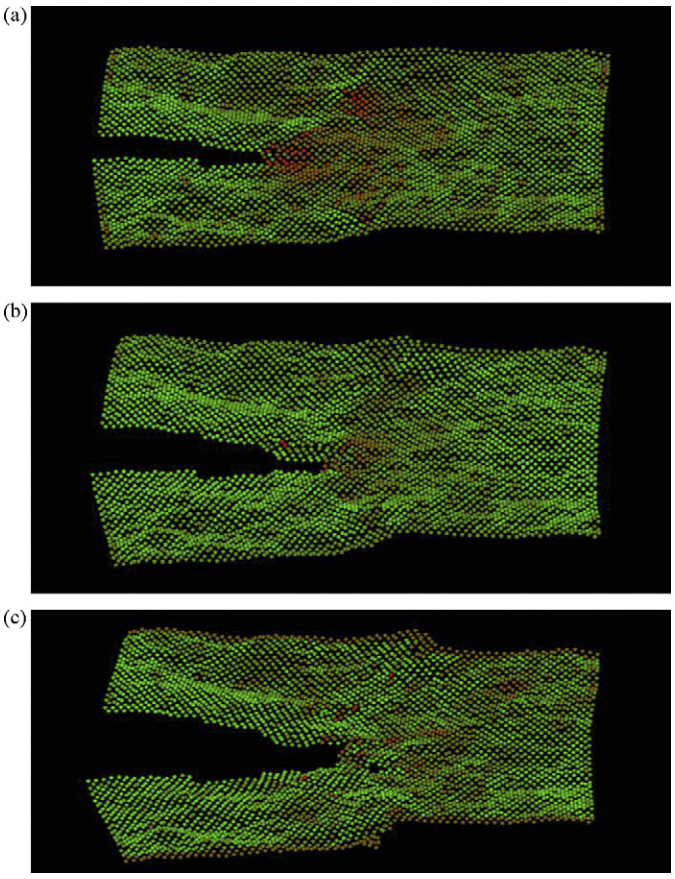

Fig. 9. Simulation snapshot of the crack propagation at three different time steps: (a) after 12 ps; (b) 19 ps; (c) 25.5 ps, with $H = 0.7$. This figure corresponds to Fig. 5 for stress rate equals to 1. The colour code is the same as Fig. 1.

Furthermore, we observe that for a small value of roughness, crack branching is more evident (cf. Fig. 7), and the bifurcation of the original crack into two daughter cracks is clearly more visible. Comparison of these figures also shows that as the roughness increases, the crack tip becomes more *blunt*, i.e. the COD increases. Fig. 9 also shows that COD increases with time. The difference in the behaviour of the crack tip observed in Figs. 7–9, as H is increased, i.e. the increase in COD, could indicate that the material becomes softer, i.e. rather than the crack tip advancing into the lattice, the COD is increased.

4.5. Discussions

In this paper we have investigated, for the first time, the propagation of a dynamic crack in a *topologically distorted* lattice, represented by a rough surface. This work can be regarded as a novel extension of the research already performed in the field of crack propagation in crystalline materials. The modelling of crack propagation in such materials performed so far, using such techniques as MD simulation, has been exclusively concerned with 2D and 3D systems that are basically free from topological distortions, such as surface roughness. Topologically distorted surfaces can manifest themselves in many areas of materials science and nano-technology devices. Indeed, most surfaces are rough at nanoscopic scales even at modest temperatures, and the investigation into the dynamics of crack propagation in such systems can provide deep insight into the mechanisms by which crack unfolds in real nano-scale structures. We have shown that the phenomena that are observed in the crack dynamics pertinent to smooth 2D surfaces and smooth 3D structures are also observed in topologically distorted rough lattices. For example, the emergence of crack-path instability during the uniform movement of the crack tip, arising as a result of velocity fluctuations, and leading to the appearance of crack branching, is also observed in the type of lattice that we have considered. This implies that these phenomena are related to the dynamics of the crack propagation rather than to the structural properties of the system in which the crack is initiated and propagated, i.e. crack instability, crack velocity fluctuations, and crack limiting velocities are common features of the crack dynamics rather than special features of the geometry of the system under study.

The MD simulations presented in this paper are also novel, vis-a-vis the previous works, in another respect. In these simulations, a practical prescription has been provided to simulate nano-scale systems containing local topological distortions. We have successfully combined an efficient technique for generating a rough surface at the nano-scale, i.e. the fractional Brownian motion method, with the standard MD simulation technique. This combination affords a computational method to study crack dynamics wherein there is a local fluctuation in the geometry.

The simulations performed in this paper have been based on a very accurate interatomic potential to model the 2D triangular lattice. The fact that we have considered a 2D system, of a rather small size, clearly imposes several constraints and can influence the types of phenomena that are observed. For example in a 2D lattice the emission of dislocation loops near the crack front, as observed in 3D modelling of crack propagation [29], can not be observed. The emission of these loops affect the further movement

of the crack front, and gives rise to such phenomenon as mechanical grooving, and the emergence of topological defects. Also a small system size can give rise to artificial reflected acoustic waves at the boundary of the lattice. These waves are generated due to the emission of phonons as the crack is advancing into the lattice. Such reflected waves can affect the dynamics of the crack tip. These effects must be studied in order to obtain a better picture of the crack propagation in rough surfaces.

References

[1] D.H. Buckley, Surface Effects in Adhesion, Friction, Wear, and Lubrication, Elsevier, Amsterdam, 1981.
[2] H. Rafii-Tabar, Modelling the nano-scale phenomena in condensed matter physics via computer-based numerical simulations, Phys. Rep. 325 (2000) 239–310.
[3] H. Rafii-Tabar, Computational modelling of tribological, adhesion, indentation, and fracture processes in nano-scale systems, in: M. Rieth, W. Schommers (Eds.), Handbook of Theoretical and Computational Nanotechnology, vol. 4, American Scientific Publishers, CA, USA, 2006, pp. 191–272.
[4] H. Rafii-Tabar, H.M. Shodja, M. Darabi, A. Dahi, Molecular dynamics simulation of crack propagation in fcc materials containing clusters of impurities, Mech. Mater. 38 (2006) 243–252.
[5] S.O. Rice, Mathematical analysis of random noise, Bell Syst. Tech. J. 24 (1945) 46–156.
[6] J.A. Greenwood, A unified theory of surface roughness, Proc. R. Soc. Lond. A 393 (1984) 133–157.
[7] Q. Tao, H.P. Lee, S.P. Lim, Contact mechanics of surfaces with various models of roughness descriptions, Wear 249 (2001) 539–545.
[8] A. Majumdar, B. Bhushan, Fractal model of elastic–plastic contact between rough surfaces, J. Tribol. -Trans. ASME 113 (1991) 1–11.
[9] C. Felgueiras, M.F. Goodchild, A comparison of three tin surface modeling methods and associated algorithms, NCGIA Technical Report 95-2, 1995, pp. 1–30.
[10] H. Hamzehpour, M. Sahimi, Generation of long-range correlations in large systems as an optimization problem, Phys. Rev. E 73 (2006) 056121–056129.
[11] H. Makse, S. Havlin, M. Schwartz, H.E. Stanley, Method for generation of long-range correlations for large systems, Phys. Rev. E 53 (1996) 5445–5449.
[12] A.P. Sutton, J. Chen, Long-range Finnis–Sinclair potentials, Philos. Mag. Lett. 61 (1990) 139–146.
[13] M.W. Finnis, J.E. Sinclair, A simple empirical *N*-body potential for transition metals, Philos. Mag. A 50 (1984) 45–55.
[14] M.S. Daw, M.I. Baskes, Semiempirical, quantum mechanical calculation of hydrogen embrittlement in metals, Phys. Rev. Lett. 50 (1983) 1285–1288.
[15] H. Rafii-Tabar, A.P. Sutton, Long-range Finnis–Sinclair potentials for fcc metallic alloys, Philos. Mag. Lett. 63 (1991) 217–224.
[16] M. Born, K. Huang, Dynamical Theory of Crystal Lattices, Clarendon Press, Oxford, 1954.
[17] D. Srolovitz, K. Maeda, V. Vitek, T. Egami, Structural defects in amorphous solids. Statistical analysis of a computer model, Philos. Mag. A 44 (1981) 847–866.
[18] K. Nishioka, T. Taka, K. Hata, Interpretation of the atomic formulae for stress and stiffness coefficients, Philos. Mag. A 65 (1992) 227–244.
[19] T. Egami, D. Srolovitz, Local structural fluctuations in amorphous and liquid metals: a simple theory of the glass transition, J. Phys. F: Met. Phys. 12 (1982) 2141–2163 (also J. Phys. F: Met. Phys. 13 (1983) 909).
[20] D. Srolovitz, K. Maeda, S. Takeuchi, T. Egami, V. Vitek, Local structure and topology of a model amorphous metal, J. Phys. F: Met. Phys. 11 (1981) 2209–2219.
[21] M.P. Allen, D.J. Tildesley, Computer Simulation of Liquids, Clarendon, Oxford, 1987.
[22] J.M. Haile, Molecular Dynamics Simulation: Elementary Methods, John Wiley and Sons Inc., New York, 1992.
[23] J.A. Zimmerman, E.B. Webb, J.J. Hoyt, R.E. Jones, P.A. Klein, D.J. Bammann, Calculation of stress in atomistic simulation, Model. Simul. Mater. Sci. Eng. 12 (2004) S319–S332.
[24] R.M. Lynden-Bell, A simulation study of induced disorder, failure and fracture of perfect metal crystals under uniaxial tension, J. Phys.: Condens. Matter 7 (1995) 4603–4624.
[25] E.E. Gdoutos, Fracture Mechanics—An Introduction, Kulwer Academic, Dordrecht, Netherlands, 1993.
[26] J. Fineberg, S.P. Gross, M. Marder, H.L. Swinney, Instability in dynamic fracture, Phys. Rev. Lett. 67 (1991) 457–460.
[27] F.F. Abraham, D. Brodbeck, R.A. Rafey, W.E. Rudge, Instability dynamics of fracture: a computer simulation investigation, Phys. Rev. Lett. 73 (1994) 272–275.
[28] L.B. Freund, Dynamic Fracture Mechanics, Cambridge University Press, Cambridge, 1990.
[29] F.F. Abraham, J.Q. Broughton, Large scale simulations of brittle and ductile failure in fcc crystals, Comp. Mater. Sci. 10 (1998) 1–9.